Self-assembly via branching morphologies in nematic liquid-crystal nanocomposites

Sebastian Gurevich,[1,2] Ezequiel Soule,[3] Alejandro Rey,[2] Linda Reven,[4] and Nikolas Provatas[1]

[1]*Department of Physics, Centre for the Physics of Materials, McGill University, Montreal, Quebec, Canada*
[2]*Department of Chemical Engineering, McGill University, Montreal, Quebec, Canada*
[3]*Institute of Materials Science and Technology (INTEMA), University of Mar del Plata*
and National Research Council (CONICET), Mar del Plata, Argentina
[4]*Chemistry Department, McGill University, Montreal, Quebec, Canada*

We demonstrate that the morphological diversity in liquid-crystal hybrid systems is much richer than previously anticipated. More importantly, we reveal the existence of a dual mechanism for self-assembly of nanoparticles via morphological instabilities at phase boundaries. Using numerical simulations, we study the growth of isolated nematic droplets in an isotropic liquid crystal (LC) doped with nanoparticles (NPs) and provide insight into the nature of microstructure evolution in LC hybrids. Our work expands the numerically accessible time and length scales in these systems, capturing morphologies which develop under the competition of nonequilibrium elastic interactions, diffusive instabilities mediated by NP transport, and the anisotropy of the nematic field. By mapping nematic morphologies, we also propose a methodology for estimating various important LC material parameters that are difficult to obtain experimentally.

Self-assembly is an exciting process for patterning novel microstructures to control material functionality in a wide class of systems, ranging from quantum dots in semiconductors to carbide orientation in composite ceramics. Mixtures of liquid crystals (LCs) with nanoparticles (NPs) are an example of nanocomposites that are both of fundamental interest and can serve as a paradigm by which to better understand the process of self-assembly in nanomaterials. Directing the assembly of NPs into addressable arrangements can lead to materials with high processability, self-healing properties, and reversible control [1–3]. To date, self-assembly of NPs in these systems have been addressed in two ways: trapping in defect cores, and isotropic enrichment of NPs in micron-sized spherulitic grain boundaries. We reveal a dual mechanism where defect trapping coexists with anisotropic expulsion on the nanoscale.

The maximal elastic cost of NPs in LC is of order KR, where R is the size of the particles and $K \sim k_B T/d$ is the magnitude of the elastic modulus, which depends on the size d of the LC molecules and the local temperature T. For NPs $R \sim d$, entropic effects dominate and the particles act as molecular impurities [2]. The nematic-isotropic transition temperature decreases with the concentration of NPs and the nematic phase is partially destabilized, separating through a first-order phase transition into an isotropic phase with increased NP concentration and a nematic phase with reduced NP concentration. When coupled to the diffusive dynamics of NPs, this transition can lead to morphological instabilities of the phase boundary. Such instabilities have been reported during directional growth of pure and doped LC systems [4–8]. They are triggered by a diffusive instability of the thermal field or the impurities, respectively, which differ in their length and time scales. Free growth of nematic seeds in pure LC has been studied only up to limited length and time scales [9,10]. In contrast, free growth of nematic seeds in doped LC has remained unexplored due to the challenges associated with capturing the multiscale physics of this process. Curiously, such diffusive instabilities have been studied for more than

30 years in the context of crystal growth [11–19], being fundamental to solidification processing and microstructure evolution in metallic alloys.

Nematic textures in the presence of nanoparticles have been explored using molecular dynamics and Monte Carlo [20,21], as well as using continuum models of LCs that treat the NPs as boundary conditions [22,23]. However, atomistic models are unable to access experimentally relevant length scales, and while continuum models can capture mesoscopic structures in the nematic phase, they typically do not account for the entropy of the NPs, which is required to represent phase separation between particle rich and particle poor phases. This Rapid Communication reports mesoscale simulations of a recent multiphase theory developed to self-consistently couple the LC and NPs interactions in the continuum limit. Using an advanced adaptive mesh refinement algorithm, our simulations access a large range of length scales, allowing us to predict and map out an extended range of possible morphologies in LC-NP mixtures.

A detailed account of the model can be found in Refs. [24,25]. It represents a mixture of calamitic nematic LC (rods) and NPs (hard spheres) of comparable size. The LC can present orientational order and the NPs can present *supramolecular positional* order. Consequently, four phases can arise: isotropically dispersed particles in isotropic LC (isotropic phase), isotropically dispersed particles in nematic LC (nematic phase), ordered particles in isotropic LC (crystalline phase), and ordered particles in nematic LC (nematic-crystalline phase). The state of the mixture is characterized by the LC (NP) volume fraction ϕ ($\phi_{NP} = 1 - \phi$), the degree of positional ordering of NPs, $\sigma \in [0,1]$, and the local LC orientation, quantified by the eigenvectors of the traceless symmetric 3×3 $\mathbf{Q}(\bar{r})$ tensor, each weighted by its corresponding eigenvalue. The uniaxial order parameter $S \in [0,1]$ characterizes the local predominance of a given direction and is proportional to the leading eigenvalue. It vanishes in the isotropic phase, where $\mathbf{Q}$ vanishes.

The thermodynamics of the system is described by the (homogeneous) free energy of the mixture $f_h = f_{\text{nem}} + f_{\text{mix}} + f_{\text{crys}} + f_{\text{int}}$. The nematic free energy f_{nem}, derived from the Maier-Saupe free energy, is an expansion in rotationally invariant tensor products $\mathbf{Q} : \mathbf{Q}$ and $(\mathbf{Q} \cdot \mathbf{Q}) : \mathbf{Q}$ whose coefficients depend nontrivially on temperature and composition [26]. It is a double well potential function of S, with minima at $S = 0$ and $S \neq 0$. The entropy of mixing f_{mix} contains the Flory-Huggins entropy of mixing, and a term derived from the Carnahan-Starling equation of state for a fluid of hard spheres that accounts for excluded-volume effects. The crystalline free energy f_{crys} is based on the mean-field model of Matsuyama [27] and represents configurational entropy and excluded volume effects. Finally, f_{int} accounts for interactions between LC and NPs. It consists of a modified regular solution (Flory-Huggins) term for isotropic interactions, and an elastic-surface term accounting for elastic distortions in the vicinity of a particle. Following Ref. [25], we use values obtained by fitting experimental data from a mixture of $4'$-n-pentyl-4-cyanobiphenyl (5CB) and gold NPs coated with a mixed monolayer of short alkyl chains and n-dodecylcyanobiphenyl (12CB), and obtain the phase diagram included in Fig. 1. Although in Ref. [25] only the isotropic (I) and nematic (N) parts of the phase diagram were calculated, we include the crystalline (C) and nematic-crystalline (NC) phases.

The conserved (ϕ) and nonconserved (σ and $\mathbf{Q}$) order parameters evolve according to *model C* relaxational dissipative dynamics of the Hohenberg and Halperin classification [28],

$$\frac{\partial \mathbf{Q}}{\partial t} = -M_Q \left(\frac{\partial f_h}{\partial \mathbf{Q}} - \boldsymbol{\nabla} \cdot \frac{\partial f_g}{\partial \boldsymbol{\nabla} \mathbf{Q}} \right), \tag{1}$$

$$\frac{\partial \sigma}{\partial t} = -M_\sigma \left(\frac{\partial f_h}{\partial \sigma} - \boldsymbol{\nabla} \cdot \frac{\partial f_g}{\partial \boldsymbol{\nabla} \sigma} \right), \tag{2}$$

$$\frac{\partial \phi}{\partial t} = M_\phi \nabla^2 \left(\frac{\partial f_h}{\partial \phi} - \boldsymbol{\nabla} \cdot \frac{\partial f_g}{\partial \boldsymbol{\nabla} \phi} \right). \tag{3}$$
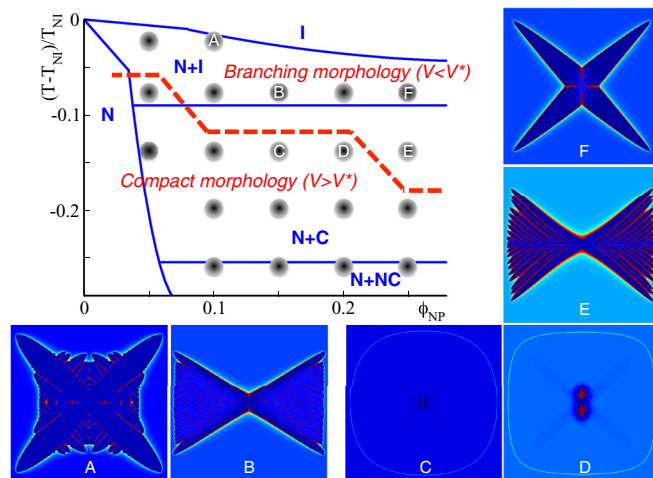

FIG. 1. (Color online) Phase diagram, quenches explored, and typical nematic morphologies (NP concentration maps). All envelope radii are above 45 μm. The dashed line marks the interface stability limit. N, I, C, and NC denote the different phases. T_{NI} is the nematic-to-isotropic transition temperature.

TABLE I. Material parameters, $\{x\} = \{\sigma, \phi, \phi Q, \phi \sigma, \sigma Q\}$ and $\{X\} = \{\sigma, Q\}$.

L_1 (J/m)	L_2 (J/m)	$L_{\{x\}}$ (J/m)	M_ϕ (m^5/sJ)	$M_{\{X\}}$ (m^3/sJ)
3.0×10^{-12}	3.1×10^{-12}	3.0×10^{-12}	10^{-13}	11.9

The gradient free-energy density f_g is given by

$$\begin{aligned} f_g = {} & \frac{L_1}{2} (\boldsymbol{\nabla}\mathbf{Q}) \overset{.}{:} (\boldsymbol{\nabla}\mathbf{Q}) + \frac{L_2}{2} (\boldsymbol{\nabla} \cdot \mathbf{Q}) \cdot (\boldsymbol{\nabla} \cdot \mathbf{Q}) \\ & + \frac{L_\sigma}{2} (\boldsymbol{\nabla}\sigma)^2 + \frac{L_\phi}{2} (\boldsymbol{\nabla}\phi)^2 + L_{\sigma Q} (\boldsymbol{\nabla}\sigma) \cdot (\boldsymbol{\nabla} \cdot \mathbf{Q}) \\ & + L_{\phi Q} (\boldsymbol{\nabla}\phi) \cdot (\boldsymbol{\nabla} \cdot \mathbf{Q}) + L_{\phi\sigma} (\boldsymbol{\nabla}\phi) \cdot (\boldsymbol{\nabla}\sigma), \end{aligned} \tag{4}$$

where L_1 and L_2 are the Landau constants coupling the elastic response to local splay bend and twist. L_3 is neglected, implying equal bend and splay responses. The cost of forming interfaces is weighted by L_ϕ and L_σ, while $L_{\phi Q}$, $L_{\phi\sigma}$, and $L_{\sigma Q}$ are coupling constants. The mobilities of ϕ, σ, and $\mathbf{Q}$ are given by M_ϕ, M_σ, and M_Q, respectively. While the values of L_1 and L_2 are well established, and M_ϕ is in the range $(10^{-14}$–$10^{-12})$ m^5/(sJ), the others are not well known. Following Ref. [25] we use the values shown in Table I.

The equations of motion are solved on a C++, finite difference, adaptive mesh refinement (AMR) algorithm based on that of Provatas *et al.* [29–31], which incorporates OPENMP parallelization. The AMR approach scales CPU time and RAM with the length [area in three dimensions (3D)] of free interfaces, allowing an enormous scaleup in computational efficiency in phase field-type models of microstructure evolution. Local refinement of the computational mesh is determined by a robust error estimator that places a threshold on each of the gradients $|\boldsymbol{\nabla}\phi| > 10^{-2}$, $|\boldsymbol{\nabla}\sigma| > 10^{-2}$, and $|\boldsymbol{\nabla}(\mathbf{Q} : \mathbf{Q})| > 10^{-4}$. Here, the physical simulation domain comprises ten levels of adaption.

We explore a range of quenches (constant, uniform temperature) and volume fractions, starting with a nematic seed in an isotropic liquid, spatially uniform volume fraction, no crystalline order throughout, and far-field boundary conditions. The $\mathbf{Q}$ tensor is initialized so that S is a two-dimensional Gaussian with a standard deviation of $\sim$20 nm whose peak rises to the equilibrium value of S. The orientation in the seed is in the x direction (the direction of the text). The computational domain represents $(100 \ \mu\text{m})^2$.

Our simulations reveal a rich variety of morphologies as the range explored spans across the absolute stability limit of the phase boundary, i.e., the upper bound of the range of growth speeds for which the phase boundary is unstable. Figure 1 shows typical morphologies obtained within the stability regions in the phase diagram. Unlike classical dendritic growth, growth anisotropy is not fixed by an underlying crystal structure. It is due to the nematic orientation and is thus a dynamic property coupled to the evolution of phase boundaries and NPs transport.

Growth develops following two regimes (Fig. 2). Regime I is dominated by the competition between orientational elasticity in the bulk and at the interface, as in pure LC systems. During growth, NPs are expelled from the nematic phase
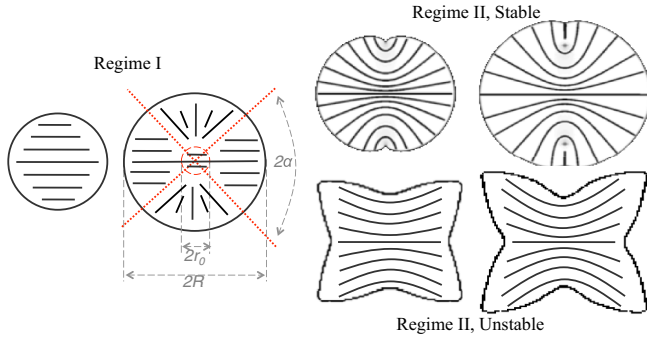
FIG. 2. (Color online) Schematic sequence of growth, characterized by two regimes. The latter can follow two growth morphologies.

and diffuse from the interface into the bulk of the isotropic liquid. Once the interface grows above the capillary length, the competition between rejection and diffusion of NPs can lead to the Mullins-Sekerka instability [11,12], which then dominates the interface shape dynamics in regime II. The bulk elasticity becomes a stabilizing effect, while anchoring at the interface provides surface tension anisotropy. Stable growth presents a compact morphology with the orientational field following closely the dynamics of pure LC nematic spherulitic growth, except that defect cores are enriched with NPs, and their size increases with NP concentration. Unstable growth presents a morphology with four main branches, which may develop secondary arms. Since the anisotropy is twofold, secondary branches may form only in the two directions of fastest growth.

Figure 3 shows the evolution of the outer radius that confines the nematic phase R for stable (unstable) growth corresponding to $\phi_{\text{NP}} = 0.25$ and $\Delta T \equiv (T - T_{\text{NI}})/T_{\text{NI}} = -0.26(-0.08)$. The early stage (regime I) is characterized by $R \smile t$, indicating that a volume driving force dominates the growth process [32]. This agrees well with previous two-dimensional (2D) droplet simulation results [33,34], and experimental results [35] that report this linear relationship for quench depths over 0.2 K. For compact morphologies the growth exponent remains unity throughout, except for a short transient period between regime I and II. For branching
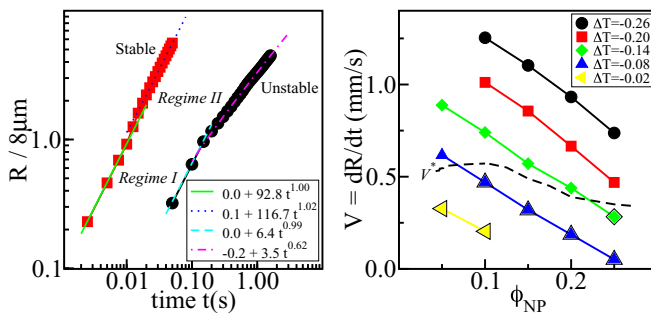

FIG. 3. (Color online) Left: Growth kinetics for stable (unstable) growth corresponding to $\phi_{\text{NP}} = 0.25$ and $\Delta T \equiv (T - T_{\text{NI}})/T_{\text{NI}} = -0.26(-0.08)$. Right: Growth rates during regime I. Outlined symbols mark cases that become unstable in regime II. The dashed line estimates V^*.

morphologies in regime II, the growth exponent is close to 1/2, characteristic of diffusion limited growth.

The early stages of pure LC nematic spherulitic growth were studied extensively by Wincure *et al.* [10,34]. The nematic droplet quickly develops the geometry outlined in regime I of Fig. 2. This geometry consists of a core with the initial orientation and two pairs of distinct regions, one with the initial orientation and the other with radial orientation. The first pair minimizes the bulk (elastic) energy at the expense of interfacial (elastic) energy, and the latter, the opposite. We can gain further insight by minimizing the total energy (bulk elasticity, surface tension, and "grain boundaries" between nematic regions) with respect to the angle α. Assuming the "grain boundaries" have an energy density of $0.5w_{\text{gb}}\sin^2(\theta)$, where θ is the angle between the orientation pairs, yields

$$(w_a R - w_{\text{gb}} r_0)\sin^2(\alpha) + (R - r_0)w_{\text{gb}}\sin(2\alpha)$$
$$= K_{11}\ln\left(\frac{R}{r_0}\right),$$

where $K_{11} = S^2(2L_1 + L_2)$ is the splay Frank elastic constant ($L_3 = 0$) and w_a is the anchoring coefficient in the Rapini-Popoular expression for surface tension $\gamma = \gamma_0 + 0.5w_a\sin^2(\varphi)$, φ being the angle between the normal to the (nematic-isotropic) interface and the local nematic orientation. The Rapini-Popoular surface tension relates to the parameters of our model as shown in Ref. [36]. For $R \gg r_0$, apart from the all-radial (outside the core) solution $\alpha = 0$,

$$\tan(\alpha) = \frac{2w_{\text{gb}}R}{w_{\text{gb}}r_0 - w_a R}.$$

Regime II starts when R is of the order of the capillary length. A larger concentration (quench) implies larger (smaller) capillary length and larger (smaller) α, in agreement with our results.

Late stage branching morphologies are triggered by the Mullins-Sekerka instability [11,12]. Sections of the interface with high positive curvature (protruding into the isotropic liquid) diffuse NPs more efficiently and speed up, while interstitial regions and interfacial sections with negative curvature become saturated in NPs and slow down, leading to the branching morphologies we observe. The morphological transition shown in Fig. 1 is the transition to absolute stability [37–40], the upper bound of this instability. Theoretical arguments [11,41–44] set it where the diffusion length becomes of the order of the capillary length, namely,

$$V^* = \frac{D\Delta T_c}{\Gamma}, \quad (5)$$

where Γ is the Gibbs-Thomson coefficient. Equation (5) assumes a diffusion controlled process with constant diffusivity D, which is related to mobility through $D = M_\phi \partial^2 f_h/\partial\phi_{\text{NP}}^2$, where gradient energy contributions to mass flux have been neglected. While $\partial^2 f_h/\partial\phi_{\text{NP}}^2$ generally depends on composition and temperature, the assumption of constant diffusivity has been shown to be reasonable for our model [24,45]. The temperature range between the nematic and liquidus lines ΔT_c is a function of the average volume fraction $\phi_{\text{NP}}^{(0)}$. Its functional form is estimated by fitting the nematic and liquidus lines with polynomials. In the dilute limit, linear liquidus
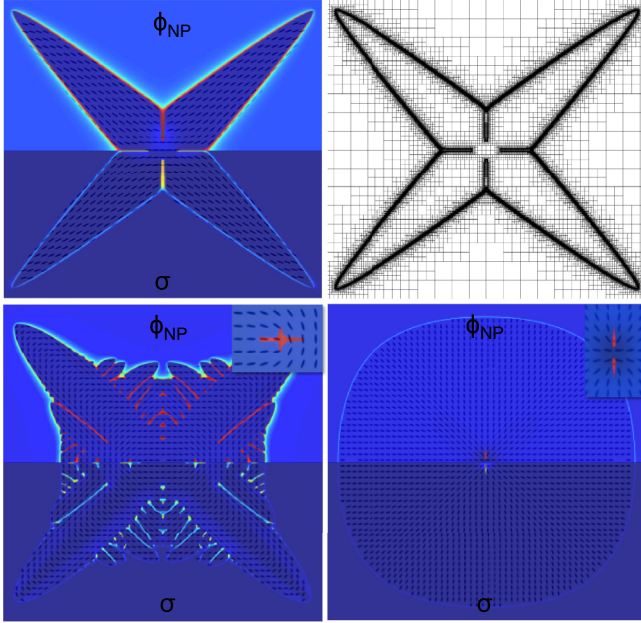
FIG. 4. (Color online) Concentration ϕ_{NP}, NP ordering (σ), and nematic orientation for $\phi_{NP}^{(0)} = 0.25$, $\Delta T = -0.08$ (top left), $\phi_{NP}^{(0)} = 0.10$, $\Delta T = -0.02$ (bottom left), and $\phi_{NP}^{(0)} = 0.25$, $\Delta T = -0.26$ (bottom right). Adaptive mesh for $\phi_{NP}^{(0)} = 0.25$, $\Delta T = -0.08$ (top right).

and nematic lines of slopes m and m/k, respectively, yield $\Delta T_c = m\phi_{NP}^{(0)}(1-k)/k$.

The growth rates $V \equiv dR/dt$ during regime I, shown in Fig. 3, are consistent with those reported by Ref. [34] in pure LC for the two-defect morphology we observe in the stable cases. Correlating the absolute stability line $V^*(\phi_{NP})$ from simulations to experimentally obtained growth rate data can provide estimates of the poorly known material parameters for such systems. For example, larger (smaller) NP mobility M_ϕ will shift $V^*(\phi_{NP})$ to higher (lower) values. Moreover, this transition could be located in experiments by controlling M_ϕ.

The dual mechanism controlling the assembly of NPs can be appreciated in the concentration maps in Fig. 1, and in more detail in Fig. 4: supersaturated NP grooves created by oriented branches and preferred segregation to localized elastic distortions (defect-core trapping). They are coupled because interfacial distortions promote defects or disclination lines, and vice versa. NPs in highly saturated regions adopt supramolecular positional ordering ($\sigma > 0$), which increases with deeper quenches, i.e., in the N+C and N+NC regions of Fig. 1.

The first quantitative theory of defect core trapping was presented in Ref. [46]. It shows that spherical NPs segregate preferentially to a defect, lower its free energy, and increase its radius with concentration, as we see in our simulations. These conclusions extend to more complex defect structures, such as disclination lines [46].

During diffusive growth, NPs rejected by the growing nematic phase accumulate in the slower moving interstitial regions of the interface. These regions become either channels as grooves deepen or regularly spaced pools entrapped by the interface. Both patterns contain highly saturated regions of NPs that can be directed through the material and process parameters that control the Mullins-Sekerka instability [Eq. (5)] and the subsequent branching morphologies we report here (Fig. 1). The latter depends on surface tension anisotropy, which itself depends on the anchoring at the interface, and can be manipulated as discussed above. Nucleation and growth of multiple nematic seeds can be further exploited to distribute NPs on extended scales through the intergrain networks that develop.

Our work reveals a self-assembly mechanism in nanocomposite LC systems that exploits the interplay between dynamic interface anisotropy, nematic elasticity, and NP diffusion. The branching morphologies we report for nematic spherulitic growth in LC-NP mixtures emerge for low quenches and high NP concentration and evolve through two regimes. At early times, the first is dominated by the elasticity of the orientational field, and the second, at later times, is dominated by a diffusive instability created by the transport of NPs. We propose systematic control of the branching morphologies, their distribution of defects and interstitial channels, as a method to control the assembly of nanoparticles. The distribution of defects can be manipulated via the initial nematic seed orientation, or the boundary conditions. Interface morphology can be manipulated either through anisotropy or the diffusive instability. Anisotropy can be controlled through the initial nematic orientation of the seed, and the diffusive instability through the material and process parameters. These can be used to promote or suppress secondary arms, which will entrap NPs in interstitial regions. This tunable organization can lead to a rich variety of structures such as NP depositions in linear disclination arrays, sheetlike arrays (large quench), and undulating dense linear structures not reported nor anticipated by basic macrosegregation methods or methods that exploit preexisting fixed defect structures.

[1] J. P. Lagerwall and G. Scalia, Curr. Appl. Phys. **12**, 1387 (2012).

[2] C. Blanc, D. Coursault, and E. Lacaze, Liq. Cryst. Rev. **1**, 83 (2013).

[3] J. Milette, S. J. Cowling, V. Toader, C. Lavigne, I. M. Saez, R. Bruce Lennox, J. W. Goodby, and L. Reven, Soft Matter **8**, 173 (2012).

[4] P. Oswald, J. Bechhoefer, and A. Libchaber, Phys. Rev. Lett. **58**, 2318 (1987).

[5] J. M. A. Figueiredo, M. B. L. Santos, L. O. Ladeira, and O. N. Mesquita, Phys. Rev. Lett. **71**, 4397 (1993).

[6] J. M. A. Figueiredo and O. N. Mesquita, Phys. Rev. E **53**, 2423 (1996).

[7] O. N. de Mesquita, Braz. J. Phys. **28**, 257 (1998).

[8] E. R. Soule, N. M. Abukhdeir, and A. D. Rey, Phys. Rev. E **79**, 021702 (2009).

[9] B. Wincure and A. D. Rey, J. Chem. Phys. **124**, 244902 (2006).

[10] B. M. Wincure and A. D. Rey, Nano Lett. **7**, 1474 (2007).

[11] W. W. Mullins and R. F. Sekerka, J. Appl. Phys. **34**, 323 (1963).

[12] W. W. Mullins and R. F. Sekerka, J. Appl. Phys. **35**, 444 (1964).

[13] M. H. Burden and J. D. Hunt, J. Cryst. Growth **22**, 99 (1974).

[14] M. H. Burden and J. D. Hunt, J. Cryst. Growth **22**, 109 (1974).

[15] J. S. Langer, Rev. Mod. Phys **52**, 1 (1980).

[16] R. Trivedi, S. Liu, and S. Williams, Nat. Mater. **1**, 157 (2002).

[17] M. Greenwood, M. Haataja, and N. Provatas, Phys. Rev. Lett. **93**, 246101 (2004).

[18] T. Haxhimali, A. Karma, F. Gonzales, and M. Rappaz, Nat. Mater. **5**, 660 (2006).

[19] S. Gurevich, A. Karma, M. Plapp, and R. Trivedi, Phys. Rev. E **81**, 011603 (2010).

[20] Z. Zhang, M. A. Horsch, M. H. Lamm, and S. C. Glotzer, Nano Lett. **3**, 1341 (2003).

[21] O. Guzman, E. B. Kim, S. Grollau, N. L. Abbott, and J. J. de Pablo, Phys. Rev. Lett. **91**, 235507 (2003).

[22] S. Grollau, E. B. Kim, O. Guzmán, N. L. Abbott, and J. J. de Pablo, J. Chem. Phys. **119**, 2444 (2003).

[23] F. R. Hung and S. Bale, Mol. Simul. **35**, 822 (2009).

[24] E. R. Soule, J. Milette, L. Reven, and A. D. Rey, Soft Matter **8**, 2860 (2012).

[25] J. Milette, V. Toader, E. R. Soulé, R. B. Lennox, A. D. Rey, and L. Reven, Langmuir **29**, 1258 (2013).

[26] E. R. Soule and A. D. Rey, Liq. Cryst. **38**, 201 (2011).

[27] A. Matsuyama, J. Chem. Phys. **131**, 204904 (2009).

[28] P. C. Hohenberg and B. I. Halperin, Rev. Mod. Phys. **49**, 435 (1977).

[29] N. Provatas, N. Goldenfeld, and J. Dantzig, Phys. Rev. Lett. **80**, 3308 (1998).

[30] N. Provatas, N. Goldenfeld, and J. Dantzig, J. Comput. Phys. **148**, 265 (1999).

[31] B. P. Athreya, N. Goldenfeld, J. A. Dantzig, M. Greenwood, and N. Provatas, Phys. Rev. E **76**, 056706 (2007).

[32] I. Dierking, Appl. Phys. A **72**, 307 (2001).

[33] Y. Lansac, F. Fried, and P. Maissa, Phys. Rev. E **52**, 6227 (1995).

[34] B. M. Wincure, Ph.D. thesis, McGill University, 2007.

[35] K. Diekmann, M. Schumacher, and H. Stegemeyer, Liq. Cryst. **25**, 349 (1998).

[36] V. Popa-Nita and P. Oswald, Phys. Rev. E **68**, 061707 (2003).

[37] W. Boettinger, D. Shechtman, R. Schaefer, and F. Biancaniello, Metall. Trans. A **15**, 55 (1984).

[38] A. Ludwig and W. Kurz, Acta Mater. **44**, 3643 (1996).

[39] W. J. Boettinger and J. A Warren, J. Cryst. Growth **200**, 583 (1999).

[40] D. Danilov and B. Nestler, Phys. Rev. Lett. **93**, 215501 (2004).

[41] W. Kurz, B. Giovanola, and R. Trivedi, Acta Metall. **34**, 823 (1986).

[42] R. Trivedi and W. Kurz, Acta Metall. **34**, 1663 (1986).

[43] P. K. Galenko and D. A. Danilov, Phys. Rev. E **69**, 051608 (2004).

[44] J. Fan, M. Greenwood, M. Haataja, and N. Provatas, Phys. Rev. E **74**, 031602 (2006).

[45] E. R. Soulé, C. Lavigne, L. Reven, and A. D. Rey, Phys. Rev. E **86**, 011605 (2012).

[46] E. R. Soule and A. D. Rey, Soft Matter **8**, 1395 (2012).